Defects Mediated Corrosion in Graphene Coating Layer
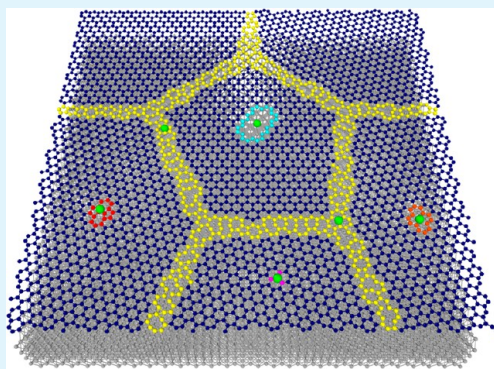
Jincheng Lei,[†,‡] Yaowu Hu,[‡,§] Zishun Liu,[†] Gary J. Cheng,[‡,§] and Kejie Zhao*[,‡]

[†]International Center for Applied Mechanics, State Key Laboratory for Strength and Vibration of Mechanical Structures, Xi'an Jiaotong University, Xi'an 710049, China

[‡]School of Mechanical Engineering and [§]School of Industrial Engineering, Purdue University, West Lafayette, Indiana 47906, United States

ABSTRACT: Mixed results were reported on the anticorrosion of graphene-coated metal surfaces—while graphene serves as an effective short-term barrier against corrosion and oxidation due to its low permeability to gases, the galvanic cell between graphene and the metal substrate facilitates extensive corrosion in the long run. Defects in the graphene layer provide pathways for the permeation of oxidizing species. We study the role of defects in graphene in the anticorrosion using first-principles theoretical modeling. Experiments in the highly reactive environment indicate that the oxidized products primarily distribute along the grain boundaries of graphene. We analyze the thermodynamics of the absorption of S and O on the grain boundaries of graphene on the basis of density functional theory. The insertion of S and O at the vacancy sites is energetically favorable. The interstitial impurities facilitate structural transformation of graphene and significantly decrease the mechanical strength of the graphene layer. Furthermore, the presence of the interstitial S and O reduces the chemical stability of graphene by enhancing the formation of vacancies and promoting dispersive growth of corrosive reactants along the grain boundaries.

KEYWORDS: graphene, protective barrier, defects, corrosion, first-principles

INTRODUCTION

Graphene is a single-atom-thick crystal of sp^2-bonded carbon that can be grown directly on metals and transferred to arbitrary substrates.[1,2] The extremely high strength,[3,4] impermeability to gases,[5−7] and chemical inertness against oxidation[8−10] make graphene an ideal anticorrosion barrier on metal surfaces. In principle, the dense hexagonal honeycomb structure in a perfect single-layer graphene (SLG) sheet would block any corrosive species.[11−13] Nevertheless, reality is that graphene prepared by chemical vapor deposition (CVD), which is widely used to grow high-quality single-layer graphene, inevitably contains a large number of atomic defects such as Stone−Thrower−Wales (STW) defects (a crystallographic defect induced by the rotation of π-bonded carbon atoms),[14] single- and divacancies, grain boundaries, nano/microvoids, and cracks.[15−19] The structural defects provide pathways for the permeation of oxidization species. A recent article reviews the use of graphene as a barrier against corrosion and highlights the effect of defects on the long-term protection.[20] The permeability can be reduced by stacking multiple layers,[21−23] yet the yield of passivation is not sufficient to prevent surface oxidation over the long term.[24] Condensed water vapor may also intercalate between graphene and the metal substrate which facilitates the wet electrochemical corrosion and results in even worse metal oxidation compared to bare substrate without SLG protection.[20,25,26] A recent novel study demonstrates that the strong graphene−metal interaction which prevents the intercalation of oxidizing species along the interface, as well as the locally formed passivating oxides near the defects of graphene, is the key in achieving the long-term protection. Another noteworthy alternative is to use hexagonal boron nitride for atomically thin protective coatings due to its insulating nature.[23,27,28] However, it was observed that the quality of the boron nitride film largely determines the level of protection,[28] and the degree of protection offered by the monolayer and multilayer hexagonal boron nitride differs in the aqueous and the air oxidative environment.[23]

The chemistry between the material defects and the corrosive species is the key to determine the degree of passivation that can be achieved by the atomically thin 2D materials. The affinity of oxidization atoms with the structural defects in 2D materials, as well as the impact of the absorbed solutes on the chemical and mechanical stabilities of the coating barrier, is largely unknown, partly because of the challenge of experimental characterization at the atomic scale and partly due to the size limit of atomistic modeling to unravel the complexity of microstructural defects in 2D materials.

We study defect-mediated corrosion through SLG using first-principles theoretical modeling. The metal substrate is not included in the work given the size limit of the atomistic modeling. Here we focus on the absorption of the oxidizing species (S and O) through the point defects and grain
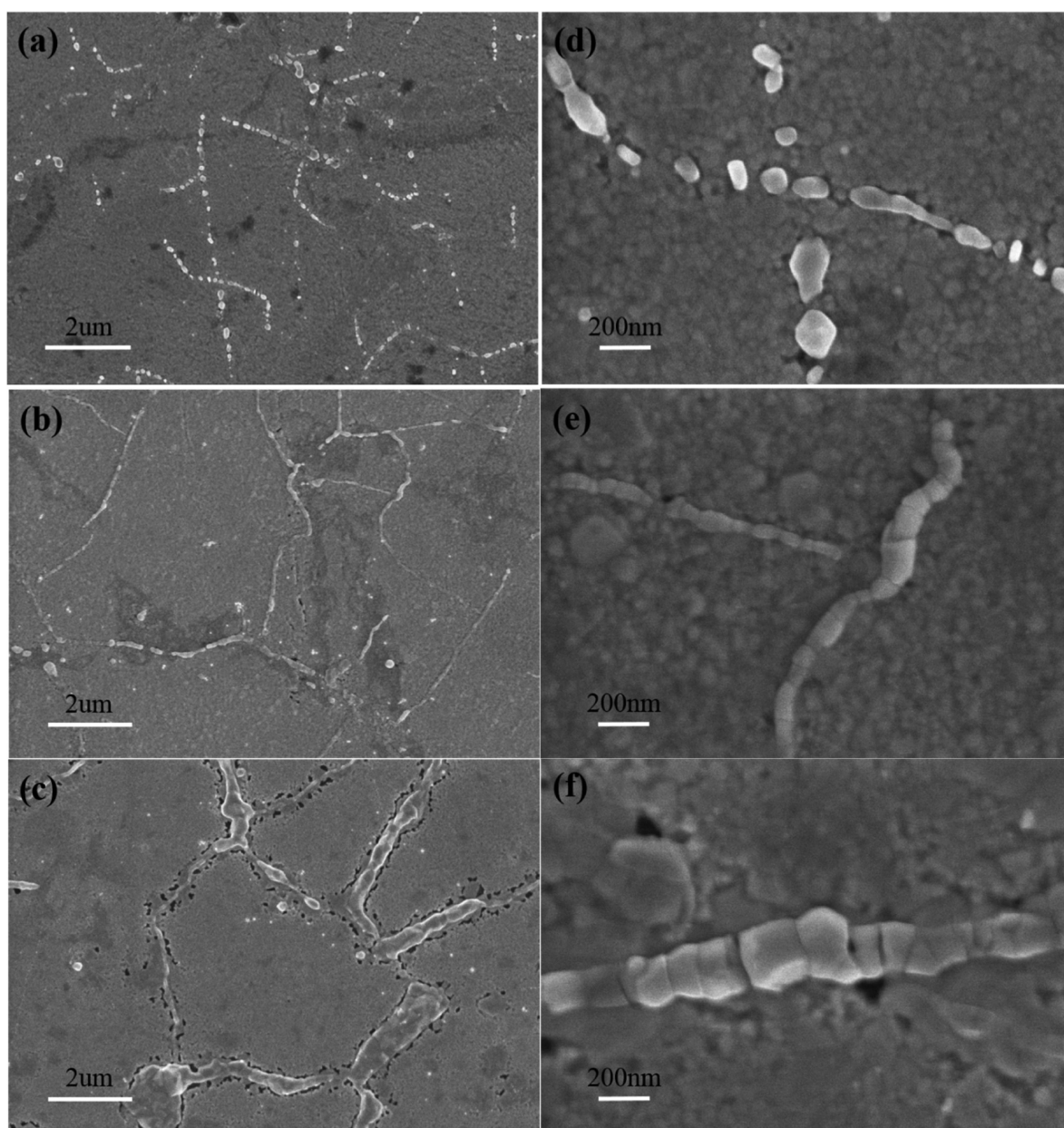
A

Figure 1. SEM images of the corrosion of Ag substrate through the grain boundary of single-layer graphene coating in the highly reactive S environment. (a)−(c) The corrosion images with exposure time 1, 2, and 3 min. (d)−(f) Local view of the sulfides in (a)−(c).

boundaries of SLG without considering the graphene−substrate interactions. Experiments in the highly reactive environment indicate that the oxidized products form and accumulate along the grain boundary of SLG. Figure 1 shows the microstructural evolution of the corroded Ag substrate covered by SLG when the sample is immersed in the S environment with the increasing exposure time. Sulfides induce a substantial amount of microvoids and cracks near the grain boundaries of SLG (Figure 1c) which further accelerate the corrosion rate. Such results are consistent with the previous observations on local oxidation of graphene along the grain bounda-ries.[12,17,20,23,25,26,29] The atomic defects (grain boundaries, vacancies, voids, cracks) in SLG provide the highway for the absorption and transport of the corrosive species, as schemati-cally shown in Figure 2. We employ first-principles modeling to study the interactions of defects in SLG with the typical oxidization atoms S and O. We demonstrate that the insertion

of S and O at the vacancy sites is thermodynamically favorable. The presence of interstitial S and O promotes structural transformation of graphene and significantly reduces the mechanical strength of SLG. Local strains associated with the structural defects in the graphene sheet also play an important role in the protection efficiency of SLG. We systematically study the strain effect on the energetics of the interstitial impurities. Furthermore, we demonstrate that the insertion of S and O reduces the chemical stability of SLG by enhancing the vacancy formation and facilitating the dispersive distribution of corrosive species along the grain boundaries.

■ COMPUTATIONAL METHODS

We use the hybrid molecular dynamics (MD) simulations and first-principles modeling to generate the atomic model of graphene with grain boundaries, and perform energetic studies in first-principles to analyze the thermodynamics of S and O insertion into the grain
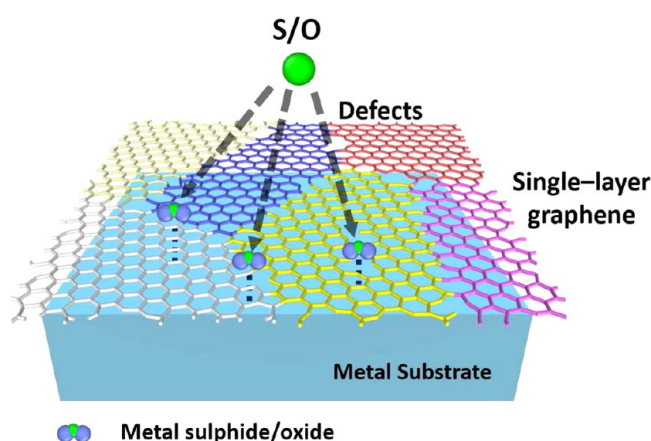
Figure 2. Schematic of the defects (grain boundaries, vacancies, voids, cracks) mediated absorption and transport of the corrosive species (S, O) through the protective graphene layer.

boundaries and explore their effects on the mechanical and chemical behaviors of graphene. The atomic model is consciously relatively small because we are interested in exploring a large number of possible configurations of defects in graphene and a wide range of perturbations of equilibrium structures through the insertion of S and O and application of strains. The choice of supercell affords our studies at a reasonable balance of computational cost, accuracy, and representation of atomic defects in 2D materials.

We first use the large-scale atomic/molecular massively parallel simulator (LAMMPS) to generate an 80-atom model by splicing two graphene sheets with a misorientation angle 21.79° in the zigzag direction. The intermolecular reactive bond order (AIREBO) potential with long-range Lennard−Jones interaction is used to describe the interactions between carbon atoms.[30,31] A dynamic simulation of 10 ps at room temperature is performed to allow carbon atoms to equilibrate at local positions, and relaxation is followed to reach the local minimum of energy. The model size is 16.24 × 13.13 Å. Periodic boundary conditions are applied in the in-plane directions. Figure 3 shows the symmetric tilt grain boundaries. The grain structure is free of dangling bonds and is composed of a perfect sp²-hybridized network of 5−7 carbon rings. It is worth noting that 21.79° is the largest misorientation angle for the zigzag-oriented grain boundaries.[32] Each
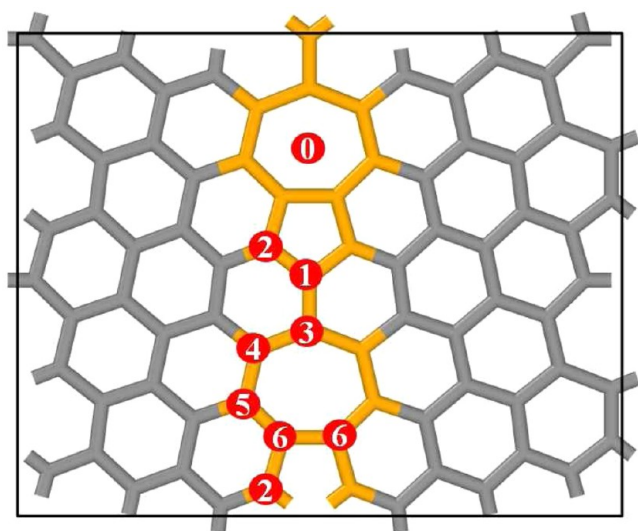

Figure 3. Atomic model of single-layer graphene with a symmetric tilt grain boundary in first-principles calculations. The misorientation angle is 21.79° in the zigzag direction. The red sites marked with numbers represent the nonequivalent positions for S/O insertion.

5−7 pair (one pentagon and one heptagon sharing one edge) is separated by one hexagon, and the resulting dislocation density is maximum in the 21.79° grain boundary. First-principles modeling is conducted using the Vienna Ab-initio Simulation Package (VASP).[33,34] Projector-augmented-wave (PAW) potentials are used to mimic the ionic cores, while the generalized gradient approximation (GGA) in the Perdew−Burke−Ernzerhof (PBE) flavor is employed for the exchange and correlation functional. The plane-wave set is expanded within an energy cutoff of 520 eV. The $3 \times 3 \times 1$ mesh of k points in the Monkhorst−Pack scheme is chosen for the Brillouin zone sampling. In energy optimization calculations, both the atomic coordinates and the supercell shape were relaxed. Energy optimization is considered complete when the magnitude of force per atom is smaller than 0.02 eV/Å.

■ RESULTS AND DISCUSSION

We first investigate the mechanism through which the oxidization atoms insert into the grain boundaries of SLG. We consider two types of occupation sites for a single S or O atom: (i) the interstitial site within the heptagon ring which has the largest volume for the insertion of guest atoms and (ii) the single vacancy site at the pentagon or heptagon ring along the grain boundary. The red spots marked with number in Figure 3 show the nonequivalent sites, where 0 represents the interstitial pentagon site and 1−6 represent the possible single vacancy site. In addition, we consider the strain effect on the energetics of absorption of S and O in graphene. Localized strains are intrinsically associated with the structural defects. Grain boundaries are subject to more strains due to the structural inhomogeneity when graphene is deformed. Furthermore, substantial strains, up to 10%, can be extrinsically induced in suspended graphene due to the bending of devices, thermal mismatch during growth, wrinkling of the graphene patch, or local nanobubbles.[35,36] The strain field alters the energy landscape of the absorption and transport of corrosive species, accelerates the formation rate of the reactants, and further causes mechanical failure of the graphene protective layer. In this study, we apply an external strain ranging from 0 to 8.3% to a given configuration to systematically map the strain effect on the S/O insertion. In the calculation of the formation energy, we take the energy of a C atom in graphene (E_C) and the energy of a S or O atom ($E_{S/O}$) in the bulk phase as the reference energies, with $E_{S/O-C}$ being the total energy of the system containing one S or O atom in the supercell which contains $80 - n$ C atoms ($n = 0$ for the interstitial heptagon site and $n = 1$ for the single vacancy site). The formation energy E_f for a single S or O atom is determined by $E_f = E_{S/O-C} - (80 - n)E_C - E_{S/O}$. The energies for a single C atom in the grain structure and for a single S and O atom in the bulk phase are −9.23 eV, −4.13 eV, and −4.94 eV, respectively.

Figure 4 shows the formation energy of an interstitial S under applied strains. The red curve represents a single S atom located within the hexagonal ring in a perfect graphene structure, and the black curve shows the comparison for the interstitial S within the heptagon ring. The insertion of S into the perfect sp²-carbon bonding network is very costly, confirming the low permeability to gases of the carbon rings. For the perfect graphene model, the formation energy linearly decreases with the applied strain indicating that the structure retains its initial configuration except bond stretching. In comparison, the interstitial S in the pentagon ring induces C bond breaking and structural transformation of the grain boundary and causes a drop of the formation energy at the applied strain of 0.06.
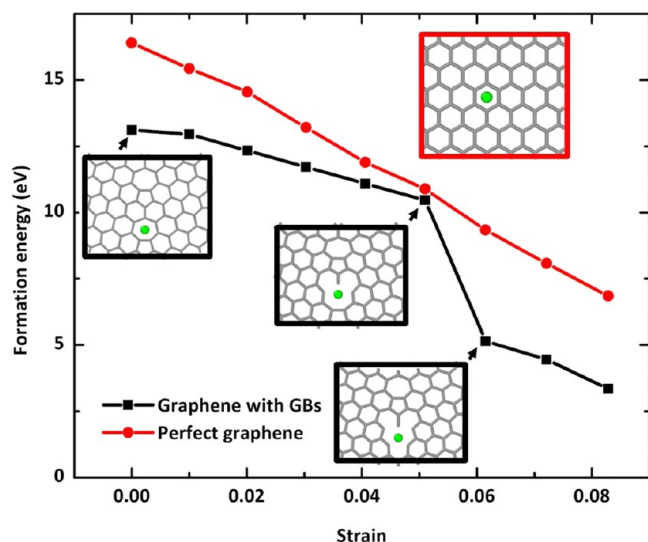
Figure 4. Formation energies of an interstitial S in the perfect graphene structure (red curve) and within the 7-ring of the grain boundary (black curve) as a function of the strain field.

Vacancies (single-, di-, and trivacancies) are the point defects well observed in carbon materials.[37,38] Vacancies maintain the intrinsic concentration at the thermodynamically equilibrium state, and a large number of vacancies can be created in graphene during the growth process or by electron/ion irradiation and chemical treatments.[39−41] The point defects have a strong influence on the electronic, optical, thermal, and mechanical properties of graphene due to the local charging states and local magnetic moments.[42,43] Here we study the effect of single vacancies at the grain boundaries on the insertion of S and O. A single vacancy is created by removing a C atom at the pentagon or the heptagon ring. Energy minimization is performed after generating a single vacancy in the carbon network. Then an interstitial S/O atom is placed at the vacancy site, and the formation energy of the single S/O atom is calculated at different applied strains. Figure 5a and b show the formation energies of an interstitial S and O at the six different vacancy sites, respectively. Overall, the formation energy of O is lower than that of S for the same configuration because of a smaller atomic volume of O. Figure 5 clearly shows that the insertion of S and O at the vacancy sites is energetically favorable—all the formation energies at the various sites are negative in the strain-free graphene except sites 1 and 2 for S. The kinks and jumps represent the drastic structural reconstruction induced by the interstitial atoms and strains in graphene. The strain effect on the energetics of S and O depends on the choice of the vacancy site. For sites 1 and 2, which are within the 5−6−6 carbon rings, the formation energy of S and O monotonically decreases (more negative) when the strain increases. The 5−6−6 rings have a compact space, and the insertion of the guest atoms is less favorable in pristine graphene. Strain increases the free volume of the interstitial impurities and thus reduces the energy barrier of S/O absorption. The atomic configurations on the right-hand outlined by the black line shows the microstructural evolution of SLG with S/O at site 1 under different strains. The 5−6−6 carbon rings remain the same morphology except the volumetric expansion with increased strains. In the cases of sites 3, 4, and 6 for S and sites 3 and 6 for O, the formation energy is weakly dependent on the strain field because the
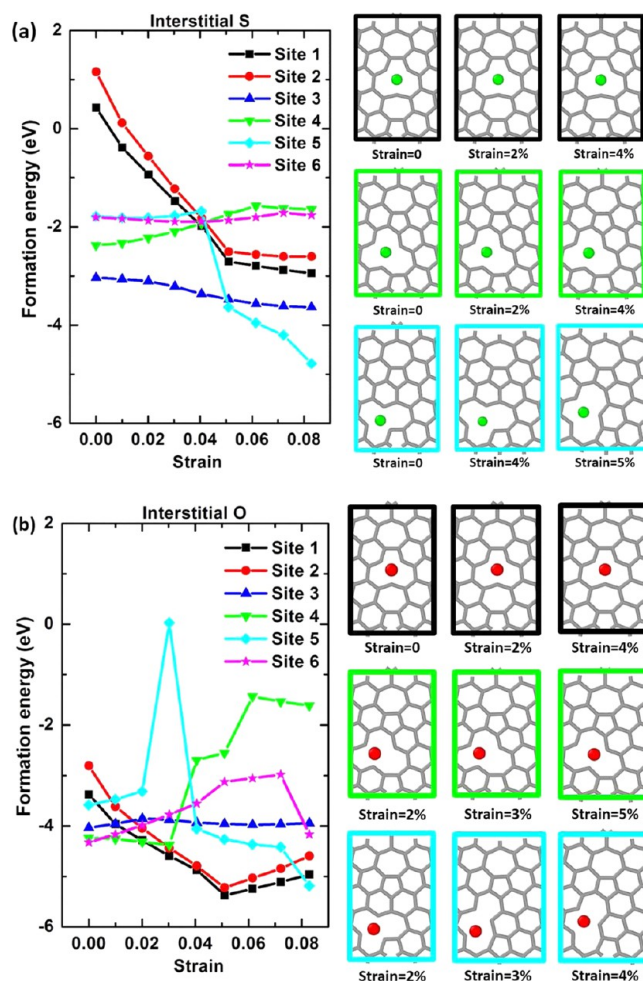

Figure 5. Formation energies of interstitial S (a) and O (b) at various single-vacancy sites under applied strains. The kinks and jumps represent the drastic structural reconstruction induced by the interstitial atoms and strains as shown in the insets. The atomic configurations show the structural transformation mediated by the interstitial S/O at a pentagon site (black line, site 1), a heptagon site (green line, site 4), and another heptagon site (cyan line, site 6).

increase in the free volume of the interstitial atoms is compensated by the decrease of the binding strength between S/O with the neighboring C atoms. The interstitial impurities and strains may induce structural transformation of graphene, and the structural reconstruction will cause a drastic change in the formation energy. Such behaviors are evident for the S insertion at site 5 and O insertion at the sites 4 and 5. The atomic configurations outlined by the cyan line show the structural evolution mediated by S/O and strains that the original 6−6−7 rings are rotated and transformed into 5−7−7 carbon rings.

The atomic defects and interstitial impurities will alter the mechanical properties of graphene. Previous studies indicate that local oxidation dramatically reduces the roughness, electric conductivity, mechanical strength, and frictional characteristics of graphene.[17,18,29] We perform uniaxial tension simulations on SLG using first-principles methods. An incremental strain is applied in the direction perpendicular to the grain boundary, and the resulting stress is recorded. Figure 6 shows the stress−strain curves of six graphene models, including perfect graphene, graphene with grain boundaries, and graphene with
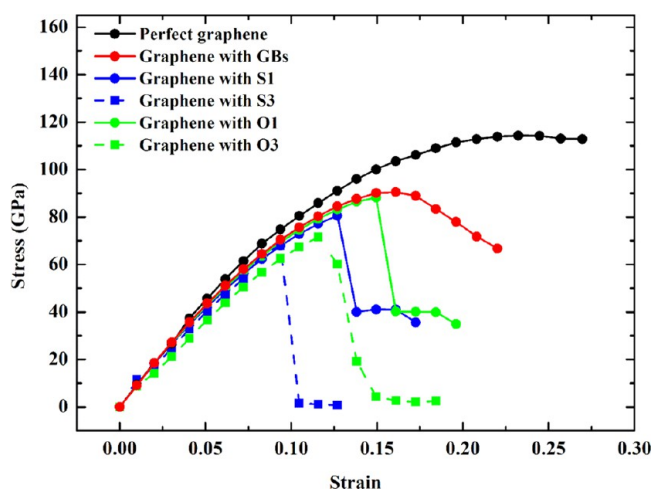
Figure 6. Stress−strain curves for different graphene models. The mechanical strength of graphene is reduced by the presence of the grain boundary and is further decreased by the insertion of the corrosive species. S1 and S3 represent graphene with one S at the interstitial sites 1 and 3, respectively; the same notation applies for O.

Figure 7. Presence of S and O promotes the formation of vacancy in graphene. (a) and (b) show the comparison of the formation energy of generating a single vacancy with and without an adjacent S and O at the pentagon (site 1) and heptagon (site 3) site, respectively. For the naming convention, V1 refers to the configuration with a single vacancy at site 1, and S3V1 refers to the configuration with one S at site 3 and a single vacancy at site 1. The same notations apply to V3, O3V1, S1V3, and O1V3.

one interstitial S/O atom at sites 1 and 3, respectively. The grain structure reduces the strength and failure strain both by roughly 20% of perfect graphene. The presence of the doping elements further reduces the strength, ductility, and elastic stiffness of graphene. S results in a larger reduction in strength than O because of the relatively stronger bonding of O−C, indicated by the formation energies in Figure 5, which retains the bonding network under strain.[44] We take the sites 1 and 3 to represent the interstitial site at the pentagon and heptagon sites. The interstitial atom at site 3 has a larger effect on the mechanical strength than that at site 1, which is consistent with the trend of the formation energy in Figure 5—vacancy at the pentagon site causes less disruption to the carbon network when graphene is deformed because of a relatively smaller void size created by the pentagon vacancy (5−6−6 ring) than the heptagon vacancy (6−6−7 ring). The simulation demonstrates that the mechanical property of graphene is highly sensitive to the defects and impurities, and the protection efficiency may be largely compromised by the loss of the mechanical stability of SLG during the corrosion process.

We further investigate the chemical stability of SLG affected by the interstitial impurities. We consider two scenarios: (i) how does the S/O atom affect the vacancy formation in the grain structures and (ii) how does the presence of the dopants influence the further absorption of the oxidization atoms. In the first case, we generate a single vacancy adjacent to the S/O atom and compare the formation energies of the single vacancy with and without the interstitial impurity. Similarly, we also compare the formation energy of one S/O atom inserted at the same vacancy site with and without an existing S/O atom at the neighboring spot. We envision that the chemical stability of SLG will be reduced by the absorbed solutes due to the facilitation of vacancy formation and dispersive growth of the oxidization products along the grain boundaries.

Figure 7 shows the formation energies of a single vacancy with and without an adjacent S/O atom. For the naming convention, V1 and V3 represent a single vacancy at site 1 (pentagon site) and 3 (heptagon site), respectively. S3V1 refers to the configuration with one S at site 3 and a single vacancy at site 1, and S1 V3 refers to the configuration with one S at site 1
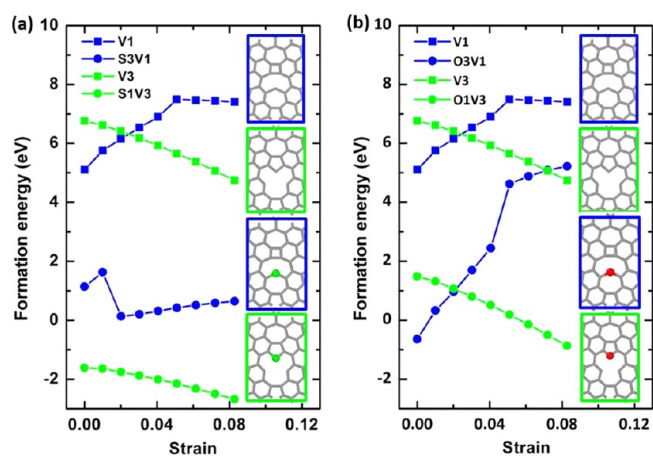
and a single vacancy at site 3. The same notation applies for O atom. The blue curves show the formation energies of a single vacancy at site 1 under applied strains. The difference in the formation energy with and without an existing S/O at the adjacent position clearly indicates that the interstitial impurities will reduce the energy barrier for the formation of point defects in graphene. Such an effect is due to the weaker S/O−C bond compared to the perfect sp^2 C−C network. In addition, the formation energy of the vacancy at site 1 becomes more positive (except a drop in S3V1 due to the structural rearrangement) when the strain increases because of the enlargement of the free volume of the vacancy in the relatively compact space of 5−6−6 rings. The formation energy of a single vacancy at site 3, represented by the green curve, again confirms that the absorption of S/O facilitates the formation of vacancies at the neighboring sites. The vacancy formation energy monotonically decreases (more negative) with the applied strain because of the dominant tension-induced weakening of the C−C bonds in the 6−6−7 rings. This might be part of the reason that voids and cracks are frequently observed near the corrosive reactants in graphene (Figure 1c) because the oxidation atoms facilitate the generation of point defects, which coalesce to create the microvoids. As the voids and cracks form, SLG quickly degrades in the chemical and mechanical stabilities and loses the protection function to the underlying substrate.

We further look into the effect of the present interstitial impurities on the consequent absorption of the corrosive atoms. This will help us understand if the corrosive products tend to accumulate at the local paths or are dispersive along the grain boundaries. Figure 8 shows the comparison of the formation energies of one S/O atom at different vacancy sites with and without an existing neighbor S/O atom. Given the many possible configurations, we do not consider the strain effect. S1 represents one S at site 1, and S3S1 represents the second S at site 1 following the insertion of one S at site 3. The same convention applies to other notations. The blue bars vs the green bars for S in Figure 8a, as well as the red bars vs the cyan bars in Figure 8b, exclusively show that the insertion of the
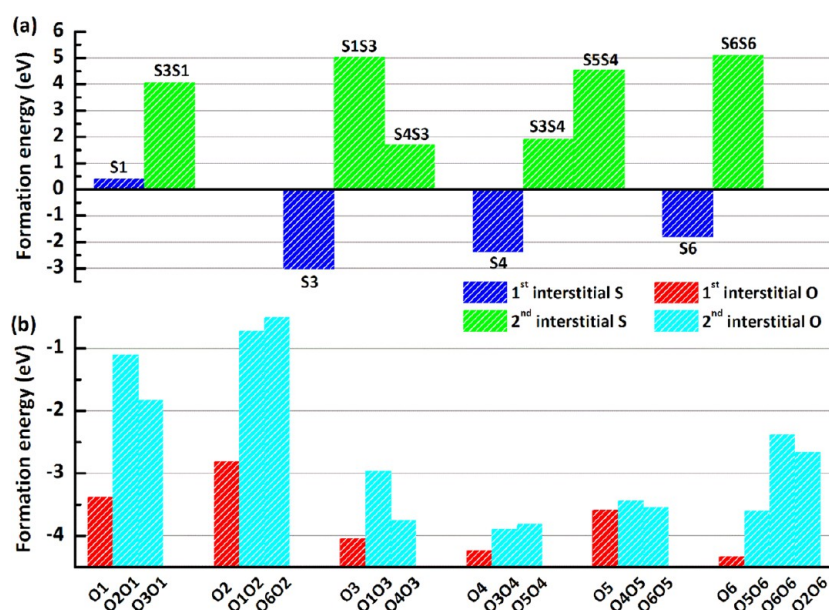
E

Figure 8. Presence of the interstitial S/O atom diminishes the thermodynamic driving force of inserting the second atom at the adjacent spot and promotes dispersive distribution of corrosive species along the grain boundary. (a) and (b) show the comparison of the formation energy of the first and second interstitial S/O atom, respectively. S1 represents one S at site 1, and S3S1 represents the second S at site 1 following the insertion of one S at site 3. The same convention applies to other notations.

second S/O atom with an adjacent guest atom is much more energetically expensive. This is due to the strong repulsion of the S−S and O−O atoms, even though the first S/O atom promotes the formation of vacancies at their neighboring site. This implies that the formation of the sulfides/oxides is more dispersive at the defective spots of graphene, which is consistent with the experimental observation (Figure 1c) that the corrosive reactants are uniformly distributed along the grain boundary.

CONCLUSIONS

Defects interact with the oxidative elements and deteriorate the long-term protective efficiency of atomically thin 2D coating barriers against corrosion. Experiments in the highly reactive environment indicate that the corrosive reactants form and grow at the grain boundaries of the graphene layer. We study the thermodynamics of the absorption of oxidization atoms in a representative grain structure of SLG using first-principles modeling. S and O insertion at the vacancy sites is energetically favorable. The interstitial impurities significantly reduce the mechanical strength of graphene and promote structural transformation under strains. Furthermore, the absorption of corrosive solutes deteriorates the chemical stability of graphene by facilitating the formation of point defects and promoting uniform growth of the reactants along the grain boundaries. This work provides valuable insight on understanding the role of defects and strain in the anticorrosion of graphene coating.

EXPERIMENTAL DETAILS

The schematic of the corrosion experiments of Ag substrate protected by a graphene layer is shown in Figure 2. A layer of Ag (100 nm) thin film is deposited on a 4 μm thick Al foil (Lebow Company Inc., Bellevue, WA) at a rate of 1 nm/s. An ultrathin Ti layer (ca. 5 nm) is utilized as the adhesion layer. Single-layer graphene (Graphene Supermarket, Inc.) grown on Cu is spin-coated with a supporting PMMA layer and baked at 150 °C for 2 min. After etching Cu by ammonium persulfate, graphene is wet-transferred to the Ag thin film. The multilayer is then naturally dried before removing PMMA with

acetone. The graphene-veiled silver thin film is exposed to S-containing environment (1 mL of aqueous ammonium sulfide ($(NH_4)_2S$) in a covered glass Petri dish (18 mm × 15 mm)) for 1, 2, and 3 min.

AUTHOR INFORMATION

Corresponding Author

*E-mail: kjzhao@purdue.edu (K. Zhao).

ORCID

Zishun Liu: 0000-0003-4669-8347
Gary J. Cheng: 0000-0002-1184-2946
Kejie Zhao: 0000-0001-5030-7412

Notes

The authors declare no competing financial interest.

REFERENCES

(1) Novoselov, K.; Geim, A.; Morozov, S.; Jiang, D.; Zhang, Y.; Dubonos, S.; Grigorieva, I. V.; Firsov, A. A. Electric Field Effect in Atomically Thin Carbon Films. *Science* **2004**, *306*, 666−669.
(2) Li, X.; Cai, W.; An, J.; Kim, S.; Nah, J.; Yang, D.; Piner, R.; Velamakanni, A.; Jung, I.; Tutuc, E.; et al. Large-Area Synthesis of High-Quality and Uniform Graphene Films on Copper Foils. *Science* **2009**, *324*, 1312−1314.
(3) Lee, C.; Wei, X.; Kysar, J.; Hone, J. Measurement of the Elastic Properties and Intrinsic Strength of Monolayer Graphene. *Science* **2008**, *321*, 385−388.

(4) Liu, F.; Ming, P.; Li, J. Ab Initio Calculation of Ideal Strength and Phonon Instability of Graphene under Tension. *Phys. Rev. B: Condens. Matter Mater. Phys.* **2007**, *76*, 064120.

(5) Bunch, J.; Verbridge, S.; Alden, J.; Van Der Zande, A.; Parpia, J.; Craighead, H.; McEuen, P. Impermeable Atomic Membranes from Graphene Sheets. *Nano Lett.* **2008**, *8*, 2458–2462.

(6) Nair, R.; Wu, H.; Jayaram, P.; Grigorieva, I.; Geim, A. Unimpeded Permeation of Water through Helium-Leak–Tight Graphene-Based Membranes. *Science* **2012**, *335*, 442–444.

(7) Leenaerts, O.; Partoens, B.; Peeters, F. Graphene: A Perfect Nanoballoon. *Appl. Phys. Lett.* **2008**, *93*, 193107.

(8) Liu, L.; Ryu, S.; Tomasik, M.; Stolyarova, E.; Jung, N.; Hybertsen, M.; Steigerwald, M.; Brus, L.; Flynn, G. Graphene Oxidation: Thickness-Dependent Etching and Strong Chemical Doping. *Nano Lett.* **2008**, *8*, 1965–1970.

(9) Surwade, S.; Li, Z.; Liu, H. Thermal Oxidation and Unwrinkling of Chemical Vapor Deposition-Grown Graphene. *J. Phys. Chem. C* **2012**, *116*, 20600–20606.

(10) Sutter, E.; Albrecht, P.; Camino, F.; Sutter, P. Monolayer Graphene as Ultimate Chemical Passivation Layer for Arbitrarily Shaped Metal Surfaces. *Carbon* **2010**, *48*, 4414–4420.

(11) Ghaderi, N.; Peressi, M. First-Principle Study of Hydroxyl Functional Groups on Pristine, Defected Graphene, and Graphene Epoxide. *J. Phys. Chem. C* **2010**, *114*, 21625–21630.

(12) Chen, S.; Brown, L.; Levendorf, M.; Cai, W.; Ju, S.; Edgeworth, J.; Li, X.; Magnuson, C.; Velamakanni, A.; Piner, R.; et al. Oxidation Resistance of Graphene-Coated Cu and Cu/Ni Alloy. *ACS Nano* **2011**, *5*, 1321–1327.

(13) Raman, R.; Banerjee, P.; Lobo, D.; Gullapalli, H.; Sumandasa, M.; Kumar, A.; Choudhary, L.; Tkacz, R.; Ajayan, P.; Majumder, M. Protecting Copper from Electrochemical Degradation by Graphene Coating. *Carbon* **2012**, *50*, 4040–4045.

(14) He, L.; Guo, S.; Lei, J.; Sha, Z.; Liu, Z. The Effect of Stone–Thrower–Wales Defects on Mechanical Properties of Graphene Sheets–a Molecular Dynamics Study. *Carbon* **2014**, *75*, 124–132.

(15) Losurdo, M.; Giangregorio, M.; Capezzuto, P.; Bruno, G. Graphene Cvd Growth on Copper and Nickel: Role of Hydrogen in Kinetics and Structure. *Phys. Chem. Chem. Phys.* **2011**, *13*, 20836–20843.

(16) Niu, T.; Zhou, M.; Zhang, J.; Feng, Y.; Chen, W. Growth Intermediates for Cvd Graphene on Cu (111): Carbon Clusters and Defective Graphene. *J. Am. Chem. Soc.* **2013**, *135*, 8409–8414.

(17) Lanza, M.; Wang, Y.; Gao, T.; Bayerl, A.; Porti, M.; Nafria, M.; Zhou, Y.; Jing, G.; Zhang, Y.; Liu, Z.; et al. Electrical and Mechanical Performance of Graphene Sheets Exposed to Oxidative Environments. *Nano Res.* **2013**, *6*, 485–495.

(18) Shi, Y.; Ji, Y.; Hui, F.; Wu, H.; Lanza, M. Ageing Mechanisms and Reliability of Graphene-Based Electrodes. *Nano Res.* **2014**, *7*, 1820–1831.

(19) Wang, H.; Maiyalagan, T.; Wang, X. Review on Recent Progress in Nitrogen-Doped Graphene: Synthesis, Characterization, and Its Potential Applications. *ACS Catal.* **2012**, *2*, 781–794.

(20) Hu, J.; Ji, Y.; Shi, Y.; Hui, F.; Duan, H.; Lanza, M. A Review on the Use of Graphene as a Protective Coating against Corrosion. *Ann. Mater. Sci. Eng.* **2015**, *1*, 16.

(21) Choi, K.; Nam, S.; Lee, Y.; Lee, M.; Jang, J.; Kim, S.; Jeong, Y.; Kim, H.; Bae, S.; Yoo, J.; et al. Reduced Water Vapor Transmission Rate of Graphene Gas Barrier Films for Flexible Organic Field-Effect Transistors. *ACS Nano* **2015**, *9*, 5818–5824.

(22) Prasai, D.; Tuberquia, J.; Harl, R.; Jennings, G.; Bolotin, K. Graphene: Corrosion-Inhibiting Coating. *ACS Nano* **2012**, *6*, 1102–1108.

(23) Jiang, L.; Xiao, N.; Wang, B.; Grustan-Gutierrez, E.; Jing, X.; Babor, P.; Kolíbal, M.; Lu, G.; Wu, T.; Wang, H.; et al. High-Resolution Characterization of Hexagonal Boron Nitride Coatings Exposed to Aqueous and Air Oxidative Environments. *Nano Res.* **2017**, 1–10.

(24) Burrows, P.; Graff, G.; Gross, M.; Martin, P.; Hall, M.; Mast, E.; Bonham, C.; Bennett, W.; Michalski, L.; Weaver, M. In *Gas Permeation and Lifetime Tests on Polymer-Based Barrier Coatings*, International Symposium on Optical Science and Technology; International Society for Optics and Photonics: 2001; pp 75–83.

(25) Schriver, M.; Regan, W.; Gannett, W.; Zaniewski, A.; Crommie, M.; Zettl, A. Graphene as a Long-Term Metal Oxidation Barrier: Worse Than Nothing. *ACS Nano* **2013**, *7*, 5763–5768.

(26) Weatherup, R.; D'Arsié, L.; Cabrero-Vilatela, A.; Caneva, S.; Blume, R.; Robertson, J.; Schloegl, R.; Hofmann, S. Long-Term Passivation of Strongly Interacting Metals with Single-Layer Graphene. *J. Am. Chem. Soc.* **2015**, *137*, 14358–14366.

(27) Li, L.; Chen, Y. Atomically Thin Boron Nitride: Unique Properties and Applications. *Adv. Funct. Mater.* **2016**, *26*, 2594–2608.

(28) Khan, M.; Jamali, S.; Lyalin, A.; Molino, P.; Jiang, L.; Liu, H.; Taketsugu, T.; Huang, Z. Atomically Thin Hexagonal Boron Nitride Nanofilm for Cu Protection: The Importance of Film Perfection. *Adv. Mater.* **2017**, *29*, 1603937.

(29) Hui, F.; Shi, Y.; Ji, Y.; Lanza, M.; Duan, H. Mechanical Properties of Locally Oxidized Graphene Electrodes. *Arch. Appl. Mech.* **2015**, *85*, 339–345.

(30) Pei, Q.; Zhang, Y.; Shenoy, V. A Molecular Dynamics Study of the Mechanical Properties of Hydrogen Functionalized Graphene. *Carbon* **2010**, *48*, 898–904.

(31) Ng, T.; Yeo, J.; Liu, Z. A Molecular Dynamics Study of the Thermal Conductivity of Graphene Nanoribbons Containing Dispersed Stone–Thrower–Wales Defects. *Carbon* **2012**, *50*, 4887–4893.

(32) Liu, T.; Gajewski, G.; Pao, C.; Chang, C. Structure, Energy, and Structural Transformations of Graphene Grain Boundaries from Atomistic Simulations. *Carbon* **2011**, *49*, 2306–2317.

(33) Kresse, G.; Furthmüller, J. Efficient Iterative Schemes for Ab Initio Total-Energy Calculations Using a Plane-Wave Basis Set. *Phys. Rev. B: Condens. Matter Mater. Phys.* **1996**, *54*, 11169.

(34) Kresse, G.; Joubert, D. From Ultrasoft Pseudopotentials to the Projector Augmented-Wave Method. *Phys. Rev. B: Condens. Matter Mater. Phys.* **1999**, *59*, 1758.

(35) Klimov, N.; Jung, S.; Zhu, S.; Li, T.; Wright, C.; Solares, S.; Newell, D.; Zhitenev, N.; Stroscio, J. Electromechanical Properties of Graphene Drumheads. *Science* **2012**, *336*, 1557–1561.

(36) Levy, N.; Burke, S.; Meaker, K.; Panlasigui, M.; Zettl, A.; Guinea, F.; Neto, A.; Crommie, M. Strain-Induced Pseudo–Magnetic Fields Greater Than 300 T in Graphene Nanobubbles. *Science* **2010**, *329*, 544–547.

(37) Yamashita, K.; Saito, M.; Oda, T. Atomic Geometry and Stability of Mono-, Di-, and Trivacancies in Graphene. *Jpn. J. Appl. Phys.* **2006**, *45*, 6534.

(38) Robertson, A.; Warner, J. Atomic Resolution Imaging of Graphene by Transmission Electron Microscopy. *Nanoscale* **2013**, *5*, 4079–4093.

(39) Hashimoto, A.; Suenaga, K.; Gloter, A.; Urita, K.; Iijima, S. Direct Evidence for Atomic Defects in Graphene Layers. *Nature* **2004**, *430*, 870–873.

(40) Krasheninnikov, A.; Banhart, F. Engineering of Nanostructured Carbon Materials with Electron or Ion Beams. *Nat. Mater.* **2007**, *6*, 723–733.

(41) Lehtinen, O.; Kotakoski, J.; Krasheninnikov, A.; Keinonen, J. Cutting and Controlled Modification of Graphene with Ion Beams. *Nanotechnology* **2011**, *22*, 175306.

(42) Ugeda, M.; Fernández-Torre, D.; Brihuega, I.; Pou, P.; Martínez-Galera, A.; Pérez, R.; Gómez-Rodríguez, J. Point Defects on Graphene on Metals. *Phys. Rev. Lett.* **2011**, *107*, 116803.

(43) Banhart, F.; Kotakoski, J.; Krasheninnikov, A. Structural Defects in Graphene. *ACS Nano* **2010**, *5*, 26–41.

(44) Lee, D.; Vlassak, J.; Zhao, K. First-Principles Analysis on the Catalytic Role of Additives in Low-Temperature Synthesis of Transition Metal Diborides Using Nanolaminates. *ACS Appl. Mater. Interfaces* **2016**, *8*, 10995–11000.